Ionics (2016) 22:1471–1483
DOI 10.1007/s11581-016-1664-7

ORIGINAL PAPER

Novel synthesis of highly porous three-dimensional nickel cobaltite for supercapacitor application

A. Nirmalesh Naveen[1,2] · **Subramanian Selladurai**[1]

Received: 14 September 2015 / Revised: 27 January 2016 / Accepted: 28 January 2016 / Published online: 10 February 2016

Abstract Highly porous 3D nickel cobaltite nanoparticles were synthesized by combustion technique. X-ray diffraction study reveals the changes in phase, crystallinity, and particle size of the prepared samples with respect to calcination temperature. Typical porous 3D foam like morphology of the materials was identified from the FESEM and HRTEM images. BET measurement further confirms the mesoporous nature of the samples with high-surface area. Mixed valence state of ions was identified from XPS measurements. Electrochemical studies disclose the impact of calcination temperature on the electrodes capacitive performance. 3D porous morphology of the material allows the complete utilization of active material available for the electrolyte ions. $NiCo_2O_4$ calcined at 400 °C exhibited the maximum specific capacitance of 908 Fg^{-1} at 5 mV/s scan rate among the prepared samples and 90 % capacitance retention at the end of 1000 cycles. Impedance study demonstrates the low resistance and facile diffusion of electrolyte ions within the material.

Keywords Calcination · Porosity · Spinel · Electrochemical capacitors

✉ A. Nirmalesh Naveen
nirmalesh.naveen@gmail.com

[1] Ionics Lab, Department of Physics, Anna University, Chennai, Tamil Nadu 600025, India

[2] St. Joseph's College of Engineering, OMR, Chennai, Tamil Nadu 600119, India

Introduction

Electrochemical devices play a crucial role in energy storage since the time of voltaic cells. Depletion of fossil fuels, the major contributors of power production and CO_2 emission have triggered the search for new and green energy producers. Transient energy available from the renewable energy sources like solar, wind, tide, etc. must be trapped efficiently for sustained energy production [1–4]. Supercapacitors or electrochemical capacitors are receiving much attention recently for their capability to store substantial amount of electrical energy efficiently. Electrochemical capacitors are far superior to conventional electrostatic capacitors and batteries in terms of energy density and power density, respectively. Owing to their rapid charge/discharge characteristic, long lifespan, reduced weight and flexibility, they are used as auxiliary power source in hybrid vehicles, short-term power sources for mobile electronic devices, ignition system, and other areas where burst of energy is required in short time [5–8]. Based on the type of charge storage mechanism, supercapacitors are classified into (i) Electric Double Layer Capacitors (EDLC) and (ii) Pseudocapacitors. Carbon-based materials store electrical energy at the electrode-electrolyte interface the basic principle of EDLC capacitors, while pseudocapacitance is found in multivalent transition metal oxides and conducting polymers that can undergo redox reaction in electrolytes [9–14]. Noble metal oxides like RuO_2 and IrO_2 exhibit much higher specific capacitance than carbonaceous materials and conducting polymers. But their application is hindered by cost effectiveness and toxicity of the materials [15–18]. Currently, various transition metal oxides like Co_3O_4 [19], NiO [20], MnO_2 [21], Fe_2O_3 [22], V_2O_5 [23], etc., and their mixed oxides are used as electrodes for supercapacitors [24]. Among them, nickel cobaltite ($NiCo_2O_4$) has previously demonstrated some remarkable electrochemical properties. Generally, nickel cobaltite is a

pure spinel oxide material in which nickel ion occupies the octahedral site and cobalt is distributed over both octahedral and tetrahedral sites and is expected to show better redox chemistry than the two single component metal oxides due to the synergistic contribution from nickel and cobalt ions. $NiCo_2O_4$ has been widely used in magnetic materials, electro-catalysts, optical limiters and switches, chemical sensors and lithium ion batteries [1]. To be a successful electrode material for supercapacitor, it must possess certain traits like small particle size, porosity, high surface area and good electro-activity. Many methods have been developed to synthesize nickel cobaltite with desirable features for facile redox process largely including hydroxide decomposition, nanocasting, electro-deposition, co-precipitation, sol–gel synthesis and hydrothermal synthesis [25]. Most of them have drawbacks in that they are energy consuming, lengthy, and involve multiple steps. It is well known that fundamental and physicochemical properties of cobaltite systems are subject to change with the method of preparation, composition of oxide and temperature of thermal decomposition. By varying the calcination temperature one can easily tune the intrinsic property of the material like crystallinity, particle size, surface area, etc. thereby having control over the electrochemical performance of the electrode material. Three-dimensional mesoporous structures are most desirable for supercapacitor applications because the porous structure offers high interior space for the facile diffusion of electrolyte ions within bulk of the material to avail the interior reactive species. Hence, there has been large amount of research interest in the preparation of metal or metal oxide with porous structures and high surface area for supercapacitor applications. Combustion synthesis or self-propagating high-temperature synthesis is an effective, low-cost method for the preparation of nanomaterials, industrialization of combustion synthesis has been realized [26]. It is widely employed for the synthesis of spinel ferrites for ceramic applications. Combustion is a robust and facile technique to prepare high crystalline nanoparticles with large surface area and porosity. According to the propellant chemistry, for a complete combustion reaction to take place, a stoichiometric molar ratio of the metal nitrate and the fuel is required ($\phi = 1$; oxidizer/fuel). The total valences of metal nitrates (oxidizer) should be balanced by the valences of complexant (fuel). By varying the fuel to oxidizer ratio, one can control the flame time and its effect on the formation, growth of the phase, and the particle agglomeration. The stoichiometric amount of fuel is altered in order to achieve the desired phase, cases where the fuel amount is reduced below this amount ($\phi < 1$) is called fuel lean and where it is above is called fuel rich ($\phi > 1$). One of the advantages of combustion synthesis is the rapid decomposition of complexant at low temperature with simultaneous evolution of large amount of gases. Low decomposition temperature and evolution of gases results in a high degree of nucleation and slow growth rate of the particles favoring the formation of nearly mono-dispersed nanoparticles [27, 28]. To the best of our knowledge, there is only a single report on the synthesis of nickel cobaltite by combustion method characterized for infrared transparency and RF absorption applications [28]. Depending on the type of fuel used for the combustion process, obtained nanoparticle properties changes drastically. Various reaction conditions influence defect concentration in the spinel lattice, thus could have an impact on charge carrier transport properties. Final stoichiometry of the product is dependent on the complexation ability of the fuel. Citric acid is most frequently used in producing large variety of ferrites via sol–gel autocombustion method because it is an inexpensive and more effective complexing agent than hydrazine and glycine in producing smaller particle-size ferrite powders.

In the present investigation, we report the synthesis of highly porous three-dimensional $NiCo_2O_4$ nanoparticles by combustion method using citric acid as fuel. This is a first time report on synthesis of phase pure nickel cobaltite nanoparticles using citric acid as fuel via combustion method for supercapacitor applications. The aim of the present work is to prepare porous nickel cobaltite nanoparticles using this novel technique and evaluate its electrochemical performance with respect to change in crystallinity, particle size, morphology, and surface properties for different calcination temperatures. Prepared materials were subjected to structural, chemical, and electrochemical characterizations to evaluate its ability for supercapacitor applications and reported below.

Experimental

Materials

Nickel nitrate ($Ni(NO_3)_2 \cdot 6H_2O$) (98 % Alfa Aesar), cobaltous nitrate ($Co(NO_3)_2 \cdot 6H_2O$) (98 % Alfa Aesar), nitric acid and citric acid (99 % Merck) were used. All the chemicals are of analytical grade and used as purchased.

Synthesis of highly porous nickel cobaltite

This typical synthesis process is facile and highly rapid, where the entire synthesis process is completed within 6 to 8 h. Stoichiometric proportions of nickel nitrate hexahydrate (0.125 M) and cobaltous nitrate hexahydrate (0.25 M) were dissolved in 20 ml of water separately and mixed together under stirring for 20 min. To this mixture, 5 mL of nitric acid was added and stirred for 10 min to obtain a homogenous clear solution. To the above mixture, 0.74 M of citric acid was added as the fuel. Here, fuel-rich stoichiometric proportion

was chosen to obtain the phase pure product. The above solution was stirred under heating till the gel-like solution is formed. After 1 h, the reaction vessel is transferred to a preheated hot plate for removing the residual water and commencement of combustion reaction. After a short while, self-combustion takes place with the decomposition of citric acid releasing large amount of gas and heat. Graphical representation of the preparation method is presented in Scheme 1. To investigate the effect of crystallinity on the properties of $NiCo_2O_4$, calcinations were performed by heating the as-prepared sample at 350, 400, and 500 °C separately under air for 4 h. The prepared compound was labeled according to their calcination temperature as NiCo-350, NiCo-400, and NiCo-500.

Physical characterization of the samples

X-ray diffractogram of the samples was recorded by Bruker X-ray diffractometer model. D2 PHASER Kα radiation of copper target with a wavelength of 1.5416 Å was used as X-ray source. Detected diffraction angle (2θ) was scanned from 10 to 80° with a step size of 0.02°. FTIR spectra of the samples were recorded between 500 and 4000 cm^{-1} wave number using FTIR spectrophotometer (Bruker). Thermogravimetry analysis (Waters model no. SDT Q600) was carried out with a heating rate of 10 °C/min scanned between room temperature and 1000 °C under nitrogen gas flow of 100 mL per minute. Morphology of the prepared samples was imaged using FEI Quanta FEG 200-Field Emission Scanning Electron Microscope (FESEM). The specific surface area measurement of the prepared compound was performed via ASAP 2020 version 4.01 with liquid nitrogen (77 K) as absorbate. X-ray photoelectron spectra were recorded using Kratos AXIS Ultra DLD X-ray photoelectron spectrometer with aluminum anode (monochromatic Kα X-rays of energy 1.486 eV) as source and operating at 160 eV pass energy. All binding energy values were charge-corrected to the C 1s signal which was set at 284.6 eV. XPS spectra were analyzed and fitted using CasaXPS software (version 2.3.16).

Fabrication of electrode and electrochemical performance test

Prepared electrode material, activated carbon, and polyvinylidene fluoride (PVDF) binder were mixed together in the ratio of 85:5:10 (wt. %). A slurry of the mixture was made using *N*-methyl-2-pyrrolidone (NMP), which was coated onto a nickel foil current collector of (1 × 1 cm) 0.25 mm thickness (produced by Alfa Aesar) and dried for 4 h to remove the solvent. The mass of the loaded samples lies within the range of 0.4–0.5 mg measured using a Shimadzu analytical balance of accuracy 0.01 mg. Cyclic voltammetry (CV), chronopotentiometry (CP), and electrochemical impedance spectroscopy (EIS) were performed using a CHI 661C electrochemical workstation employing a standard three-electrode cell configuration with platinum wire as counter electrode and standard calomel electrode (SCE) as a reference electrode. The measurements were performed using aqueous 1 M KOH electrolyte at ambient conditions within −0.1–0.5 V potential windows.

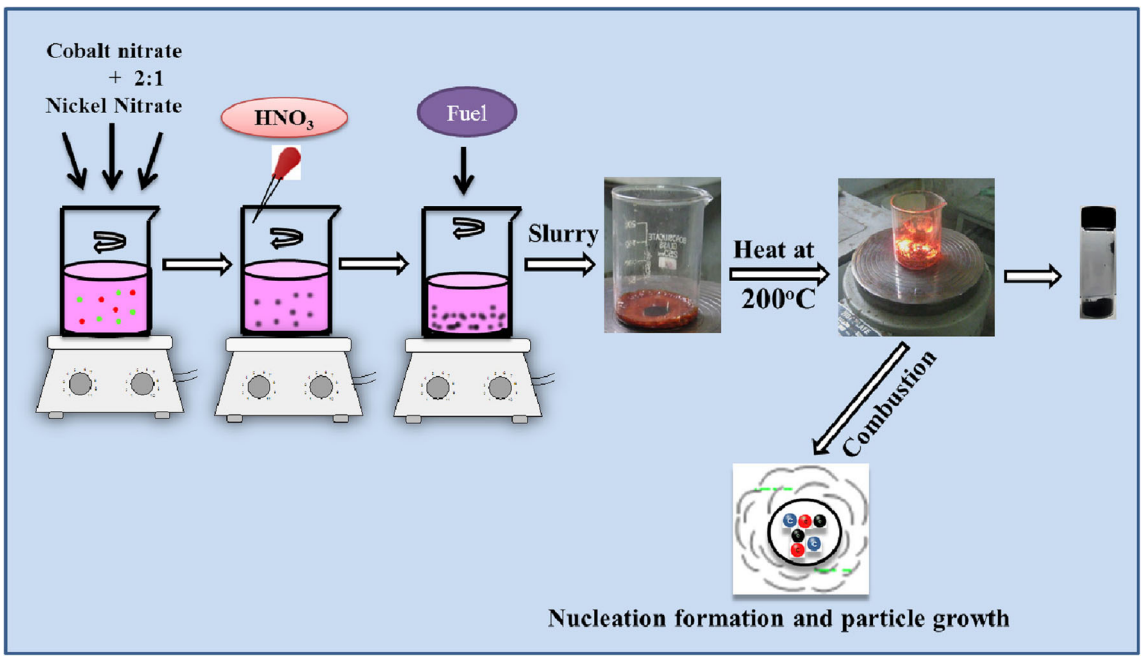

Scheme 1 Graphical representation of the preparation method

Results and discussion

Thermogravimetric analysis

Details regarding phase transition, decomposition, crystallization, and thermal stability were obtained from TG-DTA analysis, where the samples were heated from room temperature to 1000 °C. Gel obtained during the synthesis process prior to self-combustion was subjected to thermal analysis; Fig. 1 shows their TG curve along with differential curve. Three major regions of weight loss were identified from the figure. (i) Weight loss of 18 % occurred between room temperature to 152 °C accompanied with two endothermic peaks in DTA curve was due to the dehydration and evaporation of free water molecules in the gel network [29]. (ii) Total weight loss of 50 % observed in this region was due to the decomposition of nitrate–citrate complex and self-combustion reaction. Precisely at 157 °C, an exothermic peak appears with steep weight loss in TG curve marks the melting of citric acid and it decomposes strongly between the temperatures 202–224 °C. Nitrates on the other hand tend to decompose below 350 °C with the evolution of nitrogen oxides (NO, NO_2, and N_2O_3) [30]. As expected the oxidative decomposition of nitrate–citrate xerogel was strongly exothermic, evident from the intense exothermic peak at 345 °C accompanied with 29 % weight loss in the TG curve. (iii) Weight loss of 21 % noticed between 352 and 403 °C indicates the formation of nanocrystalline nickel cobaltite and further confirms the formation of crystalline nickel cobaltite below 400 °C. The broad exothermic band located at 431 °C accompanied with a meager weight loss should have come from the burning of the residual organic components [31]. A small hump seen at 488 °C can be attributed to the release of CO_2 due to decarboxylation accompanied with change in degree of crystallization. Beyond 553 °C, a small weight gain has been noticed in the TG curve (8 → 11 %), which can be attributed to the intake of oxygen from the atmosphere and possible secondary phase formation in the compound [32].

XRD studies

Structural details like phase formation, crystallinity, and particle size of the prepared samples were acquired from the XRD study. Figure 2 shows the powder XRD (PXRD) patterns of the prepared compounds. Ash collected from the combustion reaction possesses amorphous nature as revealed from the XRD pattern; phase formation occurred only when the ash was calcined at higher temperatures. PXRD pattern of the samples calcined at 350, 400, and 500 °C can be indexed to that of the pure nickel cobaltite. The resultant diffraction peaks basically corroborates with the standard patterns of cubic nickel cobaltite with spinel structure (JCPDS No. 73-1702) and cell parameter $a=b=c=8.114$ Å [24, 33]. Peaks corresponding to NiO begin to appear in the XRD pattern when the samples were calcined beyond 500 °C. $NiCo_2O_4$ was found to be in single phase only up to 500 °C, beyond which impure phases tend to distort the crystal symmetry. Average crystallite size of the prepared materials were calculated using Debye Scherrer equation given below

$$d = 0.9 \times \lambda/\beta \times \cos\theta \quad (1)$$

where, d is the crystallite size, λ is the X-ray wavelength (1.542 Å), θ is the Bragg diffraction angle and β is the full width at the half maximum (FWHM) of the diffraction peak [23]. Nickel

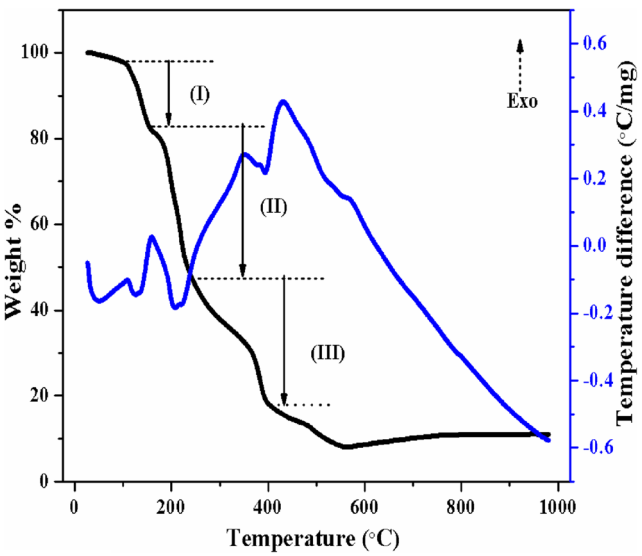

Fig. 1 TG-DTA profile of the citrate-nitrate gel obtained during synthesis

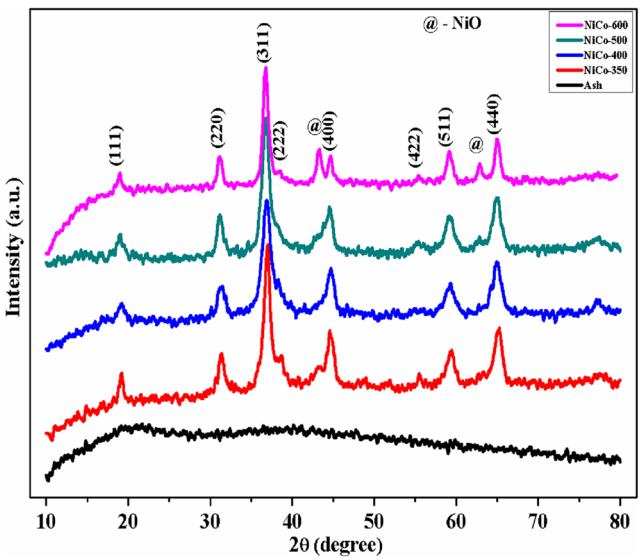

Fig. 2 Powder X-ray diffraction pattern of the samples calcined at different temperatures

cobaltite calcined at 400 °C was composed of crystallites of average size ~7 nm and it increases to ~9 nm on increasing the calcination temperature. Table 1 provides the structural parameters obtained from XRD studies. Experimentally calculated cell parameter values of NiCo-350 and NiCo-400 was lower compared to the standard value due to the presence of ion vacancies and other point defects. Elastic strain of the samples was calculated using the formula $E = \beta/2 \cot \theta$ [14]. An obvious decrease in elastic strain with an increase in particle size was noticed from Table 1. Micro straining in the lattice was due to point defects, change in bond length and bond angle caused by evolution of various gases during synthesis.

Fourier transform infrared studies

Figure 3 displays the IR spectra recorded for the samples. Nickel cobaltite's spinel formation was once again confirmed from the presence of two sharp intense absorption peaks at 557 and 649 cm^{-1}. Observed peaks were characteristics of metal oxygen stretching vibrations; the peak at 557 cm^{-1} corresponds to metal ion residing at octahedral site and the peak at 649 cm^{-1} that to metal ion at tetrahedral site in a spinel compound [34]. Absence of any absorption peak between 840 and 815 cm^{-1} was a testimony for complete decomposition of nitrates. Doublet peak at 1028 and 1101 cm^{-1} were assigned to C–O stretching vibrations. Signs of residual carboxyl group (C═O) from the fuel were found between 1300 and 1400 cm^{-1} region [35]. The peaks at 1625 and 3416 cm^{-1} were characteristics of bending vibration mode of hydrogen bonded (H–O–H) hydroxyl group and stretching vibrations arising from hydroxyl group attached to metal oxide, respectively [36]. Removal of water on increasing the calcination temperature can be noticed from the peaks corresponding to hydroxyl groups becoming less intense and weak.

Morphology investigations

Preliminary surface morphology examination of the samples was conducted using FESEM imaging technique. Images in Fig. 4 reveal the porous nature, typical for the materials prepared via combustion technique. Figure 4a and b corresponds to the low and high magnification SEM images of NiCo-350, similarly Figure 4c–d for NiCo-400 and Figure 4e–f for NiCo-500. Materials morphology was composed of a large number

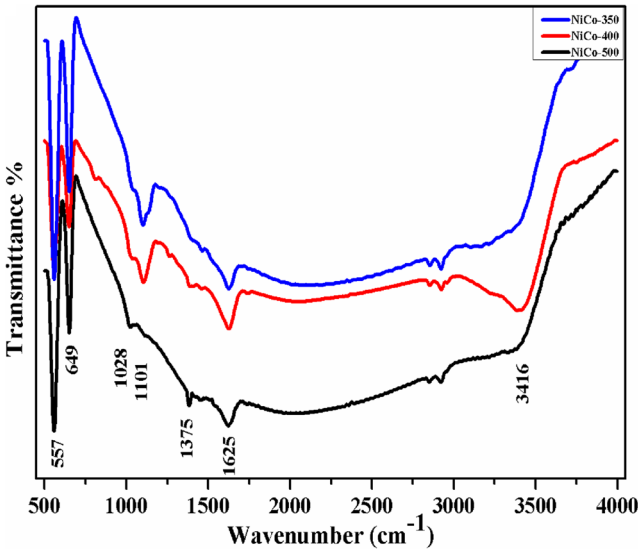

Fig. 3 Shows the FTIR of spectra of the samples calcined at 350, 400 and 500 °C

of voids and pores. High-magnification image suggest the presence of pores whose sizes ranges from mesoporous (2–50 nm) to macroporous range (>50 nm). During combustion, particle growth takes place very rapidly accompanied with the release of enormous amount of gases resulting in smaller size particles with high number of pores in the product. Figure 5a shows the TEM image of NiCo-400 depicting the 3D porous sponge like network of the prepared electrode material. Low- and high-magnification images of the sample reveal the mesoporous nature, as shown in Fig. 5b and c. Inset of Fig. 5c displays the SAED pattern recorded for NiCo-400 displaying diffraction rings corresponding to various lattice planes of the nickel cobaltite spinel system. Figure 5d shows the HRTEM image of the NiCo-400 illustrating the polycrystalline nature of the prepared sample. High specific surface area and pores of variable sizes are highly advantageous in terms of electrolyte ion transport within the material. Such pores aid in rapid supply of electrolyte ions to the bulk of the material during electrochemical reaction. As a result of facile electrolyte diffusion into the electrode material, maximum utilization of the active material can be achieved. During fast reaction rate, only surface active species react with the electrolyte ions leaving species within the bulk idle. Hence, it is important to prepare electrode materials with superior nanostructures where entire electro-active species can be utilized.

Table 1 Physical parameters of the as synthesized electrode materials

Sample name	β (FWHM)	Cell parameter $a = b = c$ (Å)	Cell volume (Å^3)	Particle size (Å)	Elastic strain E
NiCo-350	0.74614	8.07	525	112	0.002175719
NiCo-400	1.08255	8.09	529	71	0.003149988
NiCo-500	0.9332	8.12	535	89	0.002706749

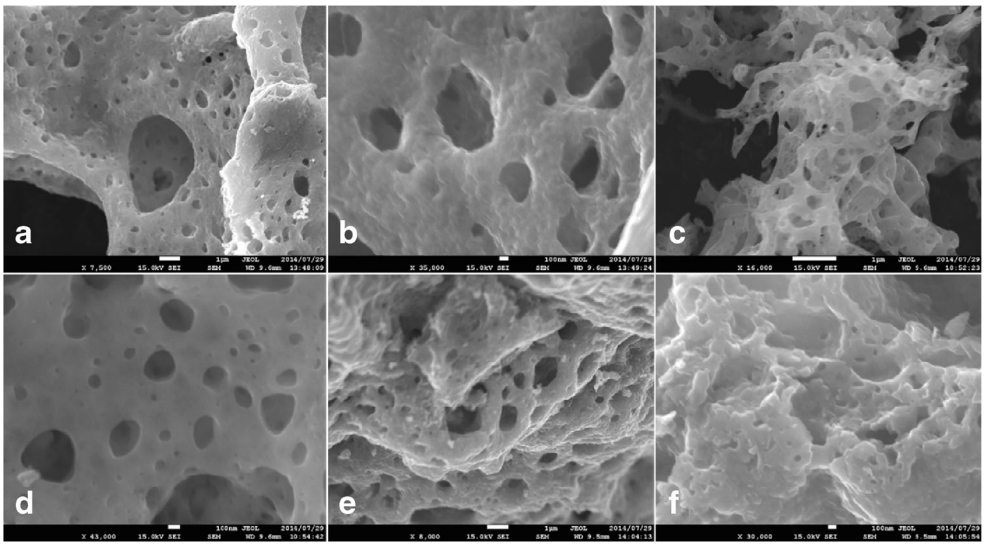

Fig. 4 The three-dimensional sponge like porous morphology of the samples at low and high magnification **a**–**b** NiCo-350, **c**–**d** NiCo-400, and **e**–**f** NiCo-500

Surface area measurements

BET measurements were carried out to study the specific surface areas and the pore structure of prepared $NiCo_2O_4$ materials. Typical nitrogen adsorption/desorption isotherm and pore size distribution of the samples are shown in Fig. 6. The nitrogen sorption isotherms of the materials can be classified as type IV with H3 type hysteresis loop behavior according to the International Union of Pure and Applied Chemistry classification [1]. The hysteresis loop observed between the wide range $P/P_0 = 0.47$ to 1 for NiCo-350, $P/P_0 = 0.4$ to 1 for NiCo-400, and $P/P_0 = 0.45$ to 1 for NiCo-500 confirms the presence of mesopores in the compound [17]. The hysteresis loop is associated with the secondary process of capillary condensation which extends up to $P/P_0 = 1$ suggesting complete filling of the mesopores and a high

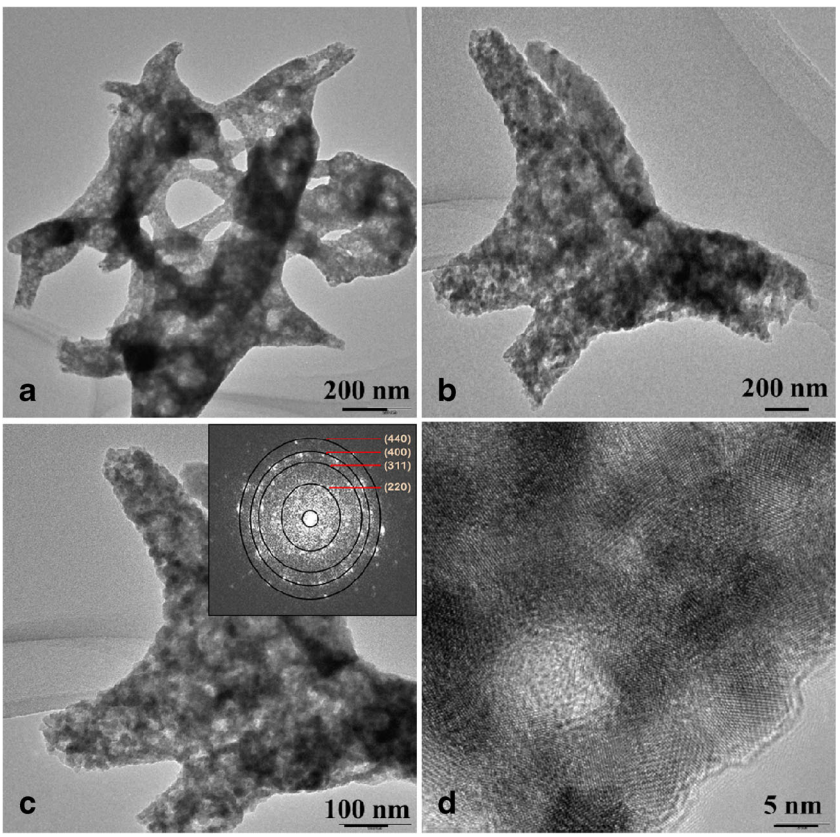

Fig. 5 **a** Shows the 3D sponge like network of the NiCo-400 nanoparticles, **b** and **c** show the mesoporous nature of the prepared sample *inset* of **c** exhibits the SAED pattern of the nickel cobaltite sample, and **d** displays the HRTEM image of NiCo-400

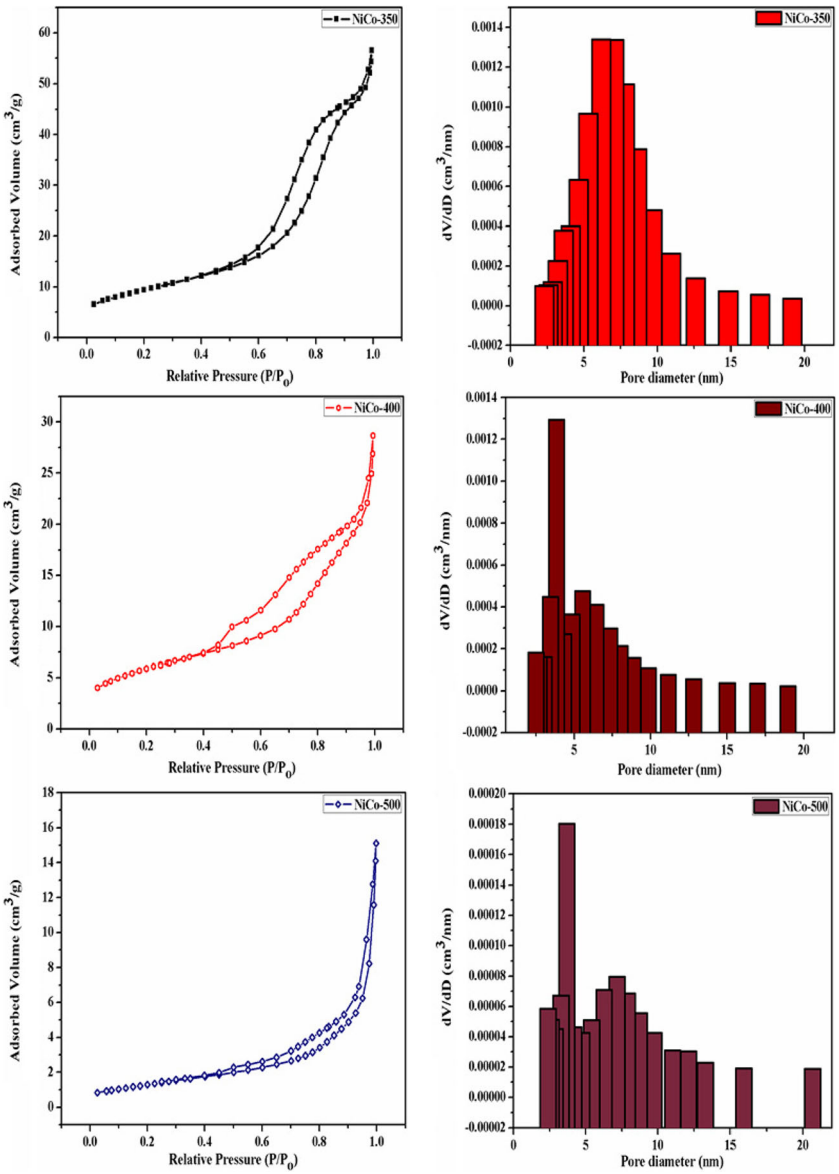

Fig. 6 N_2 adsorption/desorption isotherms of NiCo-350, NiCo-400, and NiCo-500 with their respective Barrett–Joyner–Halenda (BJH) pores size distribution

fraction of textural porosity of the materials, which is in good agreement with SEM observations. The uptake of N_2 at higher relative pressure ($P/P_0 > 0.9$) in the BET isotherm demonstrates the existence of macropores in the samples. The region beyond $P/P_0 > 0.9$ in the isotherm of NiCo-500 indicates the relatively higher amount of macropores present in the sample. Specific surface area of NiCo-350, NiCo-400, and NiCo-500 were determined as 33.8, 21.26, and 4.8 m^2/g, respectively. Decrease in surface area of NiCo-400 and NiCo-500 can be attributed to the increase in grain growth with increase in calcination temperature, as discussed in the "XRD studies" section. Large volumes of gases evolved during the combustion reaction have generated pores of wide ranges in the prepared compounds. Pore size distributions of the samples are provided adjacent to their respective isotherms. Unlike NiCo-350 that shows wide pore size distribution (5–10 nm), NiCo-400 and NiCo-500 demonstrate narrow distribution of pore sizes centering ~3.5 nm. As discussed in the thermal analysis section, heating beyond 350 °C leads to the removal of residual complexant and nitrate ions resulting in opening of mesopore channels in NiCo-400 and NiCo-500. Generally, pore sizes ranging between 2 and 5 nm are highly favorable for electrochemical processes, they are beneficial to the transport and diffusion of ions since the nanoscale pores can facilitate penetration of the electrolyte and ions through bulky electrodes [2]. Surface area measurement details of the samples were summarized in Table 2. Large specific surface area and pore volume can promote facile insertion/exertion of electrolyte ions within the electrode material and significantly increases the specific capacitance of the electrodes.

Table 2 Surface properties of the samples obtained from N_2 adsorption/desorption measurement

Sample name	BET surface area (m^2/g)	Average pore diameter (nm)	Average pore volume (cm^3/g)
NiCo-350	33.8	8.1	0.0887
NiCo-400	21.2	7.7	0.0456
NiCo-500	4.8	15.9	0.0235

XPS analysis

Detailed chemical analysis of the samples was performed using XPS and corresponding results are presented in Fig. 7a–d. Elements present on the surface of the materials were spotted in the wide spectrum. Atomic concentrations of nickel and cobalt were found close to 1: 2 ratio (Ni/Co = 0.43). Further, Co 2p spectrum was best fitted with two spin orbital doublets and two satellite peaks typical of cobalt in spinel system, using Gaussian fitting method. Peaks at 779.71 and 794.87 eV corresponds to Co $2p_{3/2}$ and Co $2p_{1/2}$ respectively with a spin orbital splitting energy of 15.16 eV along with two shakeup satellite peaks (Sat1 and Sat2) which implies the presence of two type of cobalt species (Co^{2+} and Co^{3+}) in the compound. Appearance of first satellite peak 5.53 eV above the Co $2p_{3/2}$ peak is characteristic of Co^{2+} ions and the second satellite peak 9.12 eV above Co $2p_{1/2}$ main peak is characteristic of Co^{3+} ions [14]. Similarly, for Ni 2p spectrum, two spin orbital splitting doublet main peaks and two satellite peaks were observed. Peak at lower binding energy side (855.02 eV) corresponds to Ni $2p_{3/2}$ and peak at higher binding energy (872.24 eV) corresponds to Ni $2p_{1/2}$. These main peaks along with two satellite peaks Sat 1 and Sat 2 confirm the presence of both Ni^{2+} and Ni^{3+} species [37]. Further, oxygen 1s spectrum can be deconvoluted into three constituent peaks seen in high resolution spectrum of O 1s from Fig. 7d. One, about 529.28 eV, corresponds to metal oxygen bond (M–O, M-Co, Ni), the second peak at 531.02 eV is a typical of oxygen in an OH group and strongly supports the presence of a hydroxyl species such as CoOOH and NiOOH, and the third at 532.58 eV corresponds to surface-bonded water (H–O–H) [38]. The above results are consistent with the findings from the Fourier transform infrared (FTIR) studies. These data illustrates that the surface of the as-prepared $NiCo_2O_4$ has a composition containing Co^{2+}/Co^{3+} and Ni^{2+}/Ni^{3+}. One of the difficulties regarding the crystal chemistry of spinel oxides is the determination of the metal oxidation states and cation distribution among the tetrahedral and octahedral sub-lattices sites of the spinel structure. This determination becomes more complex when two or more metallic cations with relatively similar oxidation states share the lattice sites.

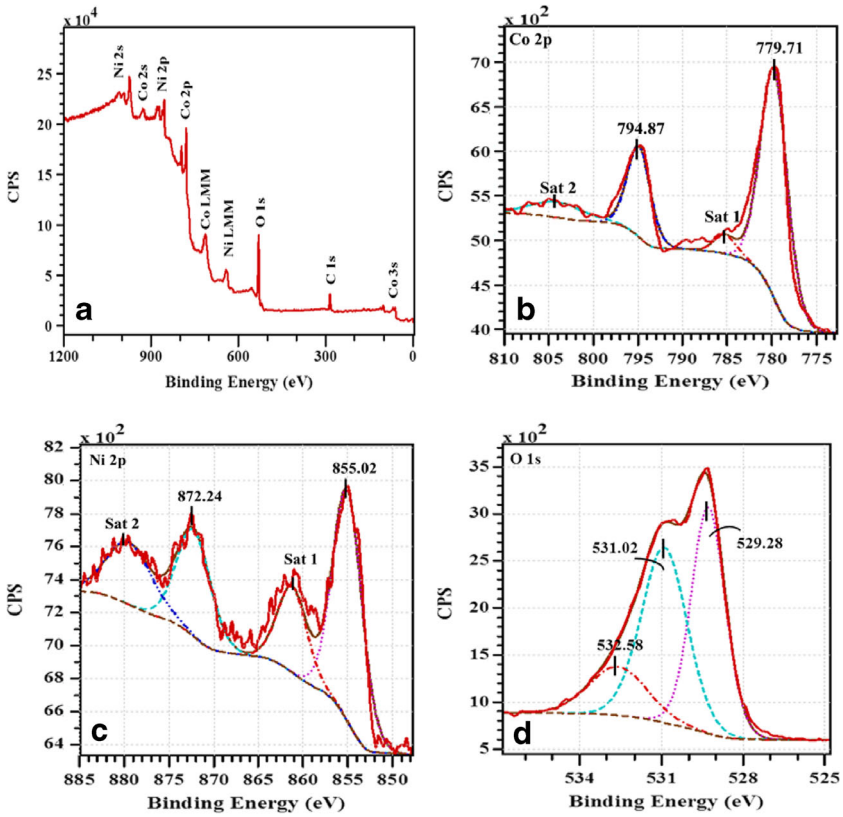

Fig. 7 **a** Elements identified from the survey spectrum of NiCo-400, **b** and **c** shows the high resolution XPS spectra of Co 2p and Ni 2p, respectively, and **d** showing resolved O 1s spectrum

Electrochemical studies

Cyclic voltammetry studies

Cyclic voltammetry (CV) is a primary technique to determine the various electrode processes, electrode reaction mechanisms, reversibility, kinetic parameters, etc. Figure 8 shows the CV performances of $NiCo_2O_4$ electrode heated at 350, 400, and 500 °C recorded at 25 mV/s scan rate in 1 M KOH electrolyte. NiCo-400 exhibits a wider potential window than other electrode material owing to its unique cation distribution. CV curve of the prepared electrode materials possesses both rectangular curve type (between −0.1 and 0.1 V) typical of double layer and distinct pair of redox peaks depicting faradaic or redox kind of charge storage mechanism. High current response observed along the redox region of the CV curve indicates that the major contribution to the capacitance was from pseudocapacitance. From the CV shape and number of redox peaks that appeared, nickel cobaltite nanoparticles prepared at different calcination temperature displays unique electrochemical performances. CV curve of nickel cobaltite heated at 350 °C shows only single pair of redox peaks compared to CV curve of NiCo-400 which possess a large anodic peak and a pair of cathodic peaks. Large anodic peak can be understood as superimposing of two anodic peaks, owing to similar and faster charge transitions of Ni and Co ions. For NiCo-500, a pair of anodic peak appears with three cathodic peaks in the CV curve. As the calcination temperature increases, crystallinity of the material improves accompanied with reduction of ions valence state and change in site occupancy leading to distinct reactivity of the materials. Nickel cobaltite is a unique inverse spinel oxide that contains nickel ions (Ni^{2+}) occupying octahedral site and cobalt ions (Co^{3+}) distributed in both tetrahedral and octahedral sites. $NiCo_2O_4$ is expected to offer richer redox chemistry than the individual single-component oxides as it contains both cobalt and nickel ions. Among the prepared materials, NiCo-400 has the highest integrated area which implies excellent electrochemical capacitive performance. The large value of current density in the voltammogram can be associated with the transition of nickel ions ($Ni^{2+}\leftrightarrow Ni^{3+}$) and cobalt ions ($Co^{2+}\leftrightarrow Co^{3+}$ and $Co^{3+}\leftrightarrow Co^{4+}$) from one state to another. The electrochemical reaction of $NiCo_2O_4$ with the electrolyte can be written as follows [25, 39]:

$$NiCo_2O_4 + OH^- \leftrightarrow NiCo_2O_4 \left|\right| OH^- + NiCo_2O_4\text{–}OH \quad (2)$$

$$NiCo_2O_4 + OH + H_2O \leftrightarrow NiOOH + 2CoOOH + 2e^- \quad (3)$$

$$CoOOH + OH \leftrightarrow CoO_2 + H_2O + e^- \quad (4)$$

These transitions are highly fast and reversible. It is very difficult to identify peaks corresponding to Ni ions and Co ions separately in the CV curve as they were identical in their reactivity. Three-dimensional network of pores developed during the synthesis have facilitated facile insertion/exertion of electrolyte ions within the bulk of the material. This provides possibility for the participation of all the active species (Ni and Co) in the electrochemical reaction resulting in multiple transitions observed in the CV curves. Scheme 2 represents graphically the import/export of electrolyte ions to the interior sites of the electrode material via open pores. Reaction rate of the material were investigated by increasing the scan rate from 5 to 100 mV/s and the results are presented in Fig. 9a–c. At high scan rates, two peaks are merged together to form a single

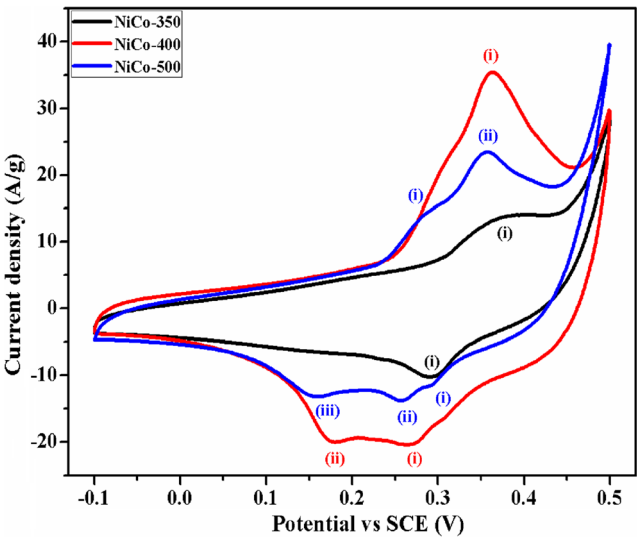

Fig. 8 CV curves recorded for the samples at 25 mV/s scan rate in 1 M KOH electrolyte

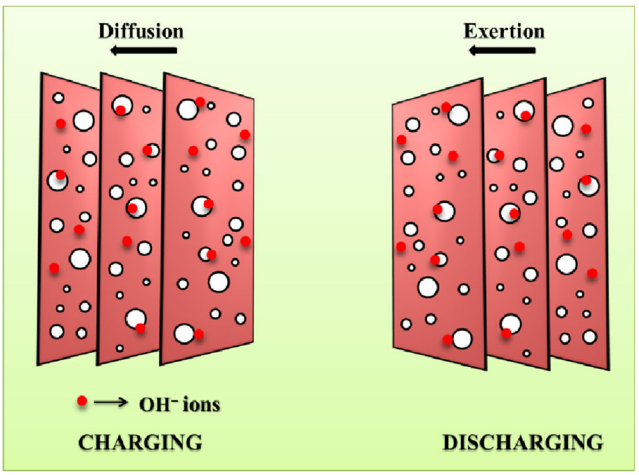

Scheme 2 Graphical representation of electrolyte ions diffusion into the interior sites of electrode material via pores during charge–discharge process

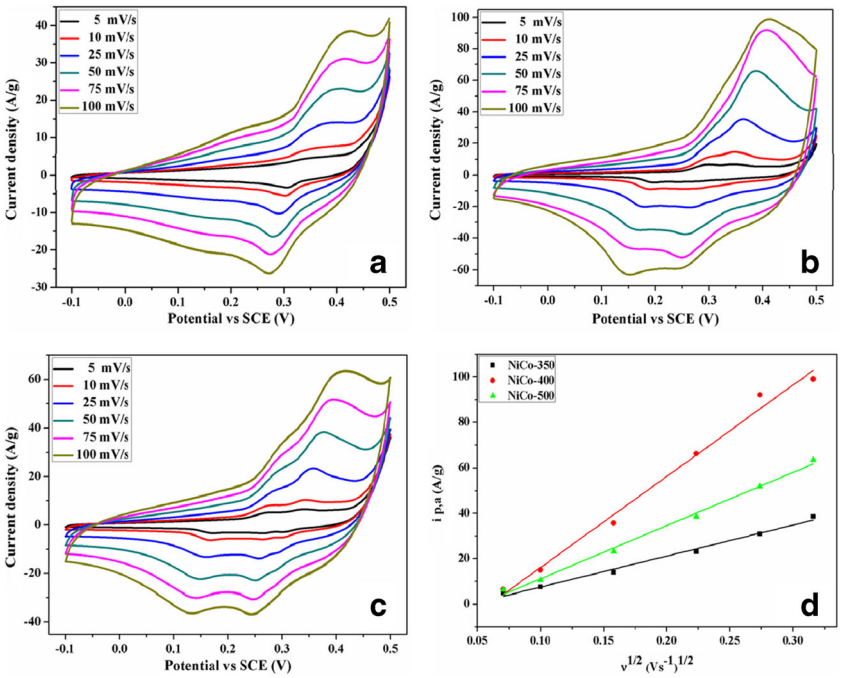

Fig. 9 (**a-c**) CV curves recorded at different scan rates (5–100 mV) for the samples calcined at 350, 400 and 500 °C and (**d**) shows the Randles – Sevcik plot of the electrode materials

broad peak in both anodic and cathodic region of the CV curves. At low scan rates, electrolyte ions have sufficient time to diffuse into the electrode material but at high scan rates, only surface ions participate in the electrochemical reaction. The increasing sweep current with the scan rate concludes the good pseudocapacitive nature of the $NiCo_2O_4$ electrodes. Randles–Sevcik plot of anodic peak current density (I p,a) versus square root of scan rate ($\nu^{1/2}$) was plotted for the samples and shown in Fig. 9d. Linear variation of peak current with scan rate denotes the diffusion controlled rate kinetics of the redox process. Among the prepared materials, NiCo-400 shows excellent capacitive behavior. Specific capacitance of the electrode materials can be estimated from the CV study using following equation:

$$SC = \frac{1}{v \times m(V_a - V_c)} \int_{V_a}^{V_c} IVdV \tag{5}$$

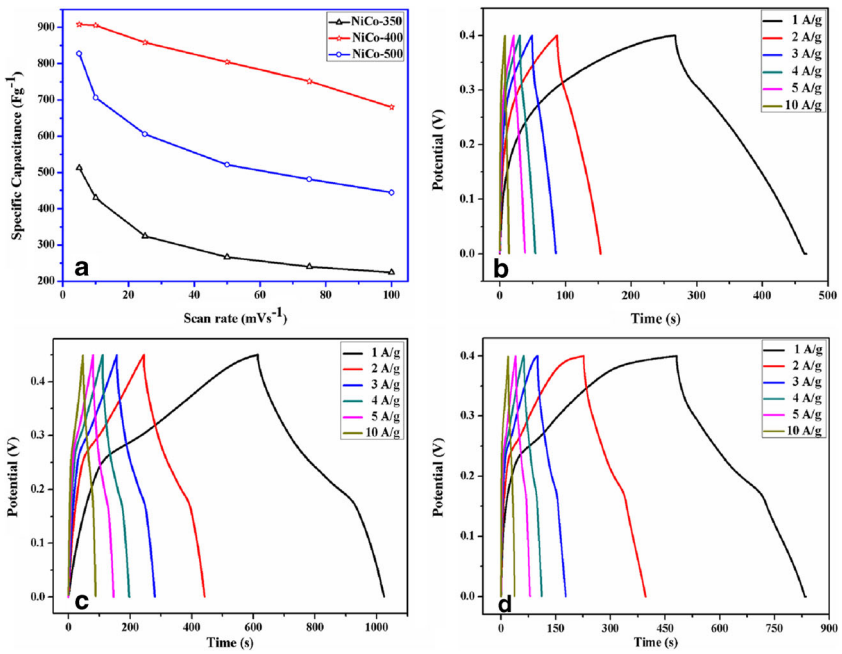

Fig. 10 (**a**) demonstrates the capacitance retention of the prepared nickel cobaltites at higher scan rates in CV measurement. (**b-d**) shows the charge – discharge profile of NiCo-350, NiCo-400 and NiCo-500 at various current density

Table 3 Quantitative measures of the electrodes capacitive performance

Sample name	SC at 5 mV/s (Fg^{-1})	SC at 1 A/g (Fg^{-1})
NiCo-350	512	497
NiCo-400	908	904
NiCo-500	827	793

The SC values were calculated graphically by integrating the area under the *I–V* curves and then dividing by the sweep rate ν ($V\ s^{-1}$), the mass of the material (m), and the potential window (V_a to V_c) [40]. Maximum specific capacitance calculated at 5 mV/s for NiCo-350, NiCo-400, and NiCo-500 was 512, 904, and 827 F/g respectively. Observed specific capacitance for the prepared materials is higher than mesoporous $NiCo_2O_4$ (554 F/g at 2 mV/s in KOH) prepared by Rui et al. [1], nickel cobaltite nanorods prepared by Rahul et al. which exhibited a maximum specific capacitance of 490 F/g [25] and hierarchical porous nanowires of $NiCo_2O_4$ obtained by Hao et al. [41]. Superior performance of NiCo-400 can be attributed to the smaller particle size that may contribute to higher capacitive performance due to the larger contact area between the electrode/electrolyte in nanostructured oxides, 3D porous foam like morphology and multiple redox species available for faradaic process. Specific capacitance calculated for other scan rates of the prepared porous nickel cobaltite electrode material is represented graphically in Fig. 10a. From the figure, NiCo-400 shows better capacitance retention at high scan rates compared to other prepared electrode materials.

Charge–discharge study

Charge–discharge characteristics of the prepared samples were investigated further using chronopotentiometry (CP) technique. Figure 10b–d shows the CP curves of NiCo-350, NiCo-400 and NiCo-500 respectively, recorded at various current densities. CP curves of the electrode materials deviate from the ideal triangular shape typical of double layer capacitance depicting the type of capacitance as pseudocapacitive, coherent with the findings from CV study. Charge–discharge curves can be clearly divided into two regions (i) A linear variation of potential with time (0–0.1 V) parallel to the vertical axis was due to the double layer capacitive behavior and (ii) a sloped variation of potential vs time (0.1–0.4 V) was due to the pseudocapacitive behavior arising from the redox activity of the species [14]. Asymmetry in the charge–discharge time suggests the irreversibility in the redox reactions. Decrease in the coloumbic efficiency can be attributed to the diffusion controlled rate kinetics of the reaction. At high current density, NiCo-400 shows maximum capacitance retention of 78 % compared to 43 and 51 % of NiCo-350 and NiCo-500 respectively. Specific capacitance can also be calculated from charge–discharge measurements using below equation:

$$SC = \frac{I \times t_d}{m \times \Delta V} \tag{6}$$

Where, I is the constant current applied, t_d is the discharge time, m is the mass of the material loaded, and ΔV is the potential difference [42]. Table 3 illustrates that specific capacitance calculated from CP, which is almost equivalent to those obtained from CV studies.

The electrochemical utilization (Z) of $NiCo_2O_4$ electrode can be calculated from the following equation:

$$Z = \frac{C_{CP} M \Delta V}{F} \tag{7}$$

Where, C_{CP} corresponds to the specific capacitances determined from CP plots, ΔV—potential window (volt), M—molecular weight of $NiCo_2O_4$(240.55 $gmol^{-1}$), and F—Faradic constant (96,487 $Cmol^{-1}$). The Z value is 1 if the entire electro-active material is involved in the redox process [42]. The Z value calculated for NiCo-350, NiCo-400, and NiCo-500 was 0.496, 0.981, and 0.790, respectively. Calculations indicate that only 50 and 79 % of the active sites

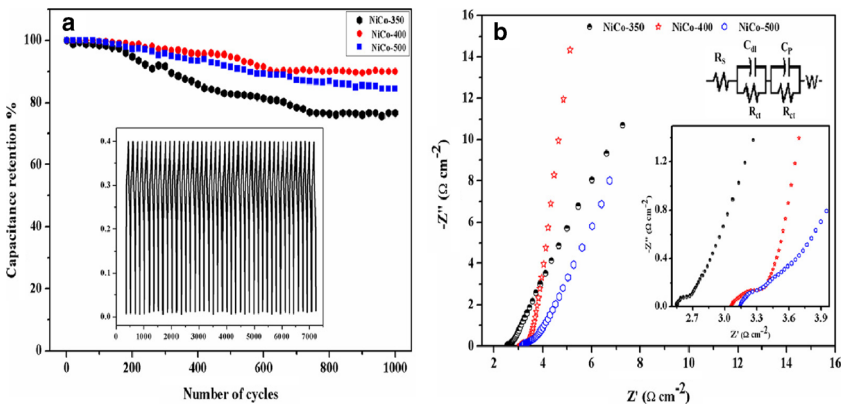

Fig. 11 (**a**) displays the capacitance retention ability over long cycling for 1000 cycles by the prepared samples and (**b**) shows the complex impedance plane (Nyquist plot) for the prepared nickel cobaltites obtained from impedance study. *Inset* of (**b**) shows the magnified portion of the high frequency region and Randle's equivalent circuit that best fits the impedance spectra

were utilized for NiCo-350 and NiCo-500, while 98 % of the sites were involved in the redox process for NiCo-400. Narrow distribution of pores size between 2 and 5 nm is responsible for the maximum electrochemical utilization and superior performance of NiCo-400. Additionally, cycling stability of the electrode materials were tested by performing charging and discharging for 1000 cycles. Figure 11a presents the result obtained from long cycling test, in which NiCo-400 exhibits maximum capacitance retention of 90 %. Its unique sponge-like morphology has reduced the strain caused by repeated insertion/exertions of electrolyte ions thereby increasing the electrode stability over prolonged cycling. Nickel cobaltite prepared by heating at 350 and 500 °C exhibits only 76 and 84 % capacitance retention.

Electrochemical impedance spectroscopy (EIS)

Information about kinetic features of the ions and electron in the electrode at the electrode-electrolyte interface are attained from electrochemical impedance spectroscopy (EIS). Samples were subjected to AC impedance measurement in the range of 1 Hz–1 MHz and the results were presented in Fig. 11b. At high-frequency region, intercept at real part of the axis gives the equivalent series resistance (ESR) or solution resistance R_S which is a sum of resistance offered by (i) charge transfer discontinuity at electrode/electrolyte interface, (ii) electrode intrinsic resistance, and (iii) contact resistance [43]. Among the $NiCo_2O_4$ samples prepared NiCo-350 show smaller ESR value of 2.55 Ω compared to 3.1 and 3.15 Ω for NiCo-400 and NiCo-500, respectively. Inset of the figure shows the near absence of semicircle in the high frequency region; diameter of the semicircle is the measure of charge transfer resistance (R_{ct}) originating from faradaic process in the electrode material. Lower internal resistance (high conductivity) is of great importance; less energy will be wasted during the charge–discharge process. Slope of the line at low frequency region gives a qualitative measurement of the resistance offered to the diffusion of electrolyte ions into the solid oxide electrode known as Warburg resistance (W) [43]. The distinctive near straight vertical line of NiCo-400 sample as compared to other heat-treated nickel cobaltite samples demonstrates lower diffusion resistance due to easy access of the OH^- ions through pores. The impedance data plots were fitted to a Randles equivalent circuit (inset in Fig. 11b). The different parameters in the equivalent circuit are characteristic of various electrochemical processes in the electrode-electrolyte interface at the specific operating frequency range. C_{dl} and C_P are double layer capacitance and pseudocapacitance that contribute to the total capacitance of the electrode materials.

Conclusions

Highly porous 3D nickel cobaltite nanomaterial has been prepared successfully via auto-combustion technique using citric acid as fuel. X-ray diffraction study reveals the change in crystallinity and particle size of the prepared samples with calcination temperature. FTIR studies further confirm the spinel nature of the compound. Mixed valence state of the ions was inferred from Ni 2p and Co 2p high-resolution XPS spectrum. Porous 3D foam like morphology of the prepared materials was confirmed from the FESEM and HRTEM images. Mesoporous nature and high surface area of the prepared materials were determined from BET measurements. Electrochemical study results reveal the impact of calcination temperature on the electrochemical performance of the electrode materials. NiCo-400 exhibits the maximum specific capacitance of 908 Fg^{-1} at 5 mV/s scan rate. Ninety percent of the original capacitance was retained at the end of 1000 cycles by NiCo-400 while 76 and 84 % were retained by NiCo-350 and NiCo-500, respectively. Impedance study demonstrates the low resistance and facile diffusion of electrolyte ions within the material. Hence, nickel cobaltite prepared by combustion technique is a potential candidate to be used as an electrode material for supercapacitor application.

Acknowledgments Financial support from Anna University by providing Anna Centenary Research Fellowship (ACRF) for A. Nirmalesh Naveen is greatly appreciated (Lr.No.CR/ACRF/2013/37).

References

1. Ding R, Qi L, Wang H (2012) A facile and cost-effective synthesis of mesoporous $NiCo_2O_4$ nanoparticles and their capacitive behavior in electrochemical capacitors. J Solid State Electrochem 16: 3621–3633
2. Su X, Yu L, Cheng G, Zhang H, Sun M, Zhang X (2015) High-performance a-MnO_2 nanowire electrode for supercapacitors. Appl Energy 153:94–100
3. Chang SK, Zainal Z, Tan KB, Yusof NA, Yusoff WMDW, Prabaharan SRS (2015) Recent development in spinel cobaltites for supercapacitor application. Ceram Int 41:1–14
4. Zhi J, Deng S, Zhang Y, Wang Y, Hu A (2013) Embedding Co_3O_4 nanoparticles in SBA-15 supported carbon nanomembrane for advanced supercapacitor materials. J Mater Chem A 1:3171–3176
5. Zhao DD, Xu MW, Zhou WJ, Zhang J, Li HL (2008) Preparation of ordered mesoporous nickel oxide film electrodes via lyotropic liquid crystal templated electrodeposition route. Electrochim Acta 53: 2699–2705
6. Zhou W, Liu J, Chen T, Tan KS, Jia X, Luo Z, Cong C, Yang H, Li CM, Yu T (2011) Fabrication of Co_3O_4-reduced graphene oxide scrolls for high-performance supercapacitor electrodes. Phys Chem Chem Phys 13:14462–14465
7. Deng JJ, Deng JC, Liu ZL, Deng HR, Liu B (2009) Influence of addition of cobalt oxide on microstructure and electrochemical capacitive performance of nickel oxide. J Solid State Electrochem 13: 1387–1394

8. Naveen AN, Selladurai S (2014) Novel synthesis of highly porous spinel cobaltite ($NiCo_2O_4$) electrode material for supercapacitor applications. AIP Conference Proceedings 1591:246–248
9. Li XG, Duan W, Huang MR, Rodriguez LNJ (2005) Electrocopolymerization of metaphenylenediamine and orthophenetidine. React Funct Polym 62:261–270
10. Li XG, Huang MR, Duan W, Yang YL (2002) Novel multifunctional polymers from aromatic diamines by oxidative polymerizations. Chem Rev 102:2925–3030
11. Li XG, Wang HY, Huang MR (2007) Synthesis, film-forming, and electronic properties of o-phenylenediamine copolymers displaying an uncommon tricolor. Macromolecules 40:1489–1496
12. Li XG, Zhang JL, Huang MR (2014) Chemical response of nanocomposite membranes of electroactive polydiaminonaphthalene nanoparticles to heavy metal ions. J Phys Chem C 118: 11990–11999
13. Li XG, Zhang JL, Huang MR (2012) Interfacial synthesis and functionality of self-stabilized polydiaminonaphthalene nanoparticles. Chem Eur J 18:9877–9885
14. Naveen AN, Selladurai S (2014) Investigation on physiochemical properties of Mn substituted spinel cobalt oxide for supercapacitor applications. Electrochim Acta 125:404–414
15. Inamdar AI, Kim YS, Pawar SM, Kim JH, Im H, Kim H (2011) Chemically grown, porous, nickel oxide thin-film for electrochemical supercapacitors. J Power Sources 196:2393–2397
16. Su X, Yu L, Cheng G, Zhang H, Sun M, Zhang L, Zhang J (2014) Controllable hydrothermal synthesis of Cu-doped α-MnO_2 films with different morphologies for energy storage and conversion using supercapacitors. Appl Energy 134:439–445
17. Jiang H, Zhao T, Li C, Ma J (2011) Hierarchical self-assembly of ultrathin nickel hydroxide nanoflakes for high-performance supercapacitors. J Mater Chem 21:3818–3823
18. Hwang SG, Ryu SH, Yun SR, Ko JM, Kim KM, Ryu KS (2011) Behavior of NiO–MnO_2/MWCNT composites for use in a supercapacitor. Mater Chem Phys 130:507–512
19. Liao M, Liu Y, Hu Z, Yu Q (2013) Novel morphologic Co_3O_4 of flower-like hierarchical microspheres as electrode material for electrochemical capacitors. J Alloys Compd 562:106–110
20. Zhang X, Shi W, Zhu J, Zhao W, Ma J, Mhaisalkar S, Maria TL, Yang Y, Zhang H, Hng HH, Yan Q (2010) Synthesis of porous NiO nanocrystals with controllable surface area and their application as supercapacitor electrodes. Nano Res 3(9):643–652
21. Jiang H, Sun T, Li C, Ma J (2012) Hierarchical porous nanostructures assembled from ultrathin MnO_2 nanoflakes with enhanced supercapacitive performances. J Mater Chem 22:2751–2756
22. Zhu M, Wang Y, Meng D, Qin X, Diao G (2012) Hydrothermal synthesis of hematite nanoparticles and their electrochemical properties. J Phys Chem C 116:16276–16285
23. Li JM, Chang KH, Hu CC (2010) A novel vanadium oxide deposit for the cathode of asymmetric lithium-ion supercapacitors. Electrochem Commun 12:1800–1803
24. Liu XY, Zhang YQ, Xia XH, Shi SJ, Lu Y, Wang XL, Gu CD, Tu JP (2013) Self-assembled porous $NiCo_2O_4$ hetero-structure array for electrochemical capacitor. J Power Sources 239:157–163
25. Salunkhe RR, Jang K, Yu H, Yu S, Ganesh T, Han SH, Ahn H (2011) Chemical synthesis and electrochemical analysis of nickel cobaltite nanostructures for supercapacitor applications. J Alloys Compd 509:6677–6682
26. Aruna ST, Mukasyan AS (2008) Combustion synthesis and nanomaterials. Curr Opinion Solid State Mater Sci 12:44–50
27. Sutka A, Mezinskis G (2012) Sol–gel auto-combustion synthesis of spinel-type ferrite nanomaterials. Front Mater Sci 6(2):128–141
28. Verma S, Joshi HM, Jagadale T, Chawla A, Chandra R, Ogale S (2008) Nearly monodispersed multifunctional $NiCo_2O_4$ spinel nanoparticles: magnetism, infrared transparency, and radiofrequency absorption. J Phys Chem C 112:15106–15112
29. Makhlouf MT, Abu-Zied BM, Mansoure TH (2013) Direct fabrication of cobalt oxide nanoparticles employing sucrose as a combustion fuel. Journal of Nanoparticles 384350:1–7
30. Ananthakumar S, Anas S, Ambily J, Mangalaraja RV (2010) Microwave assisted citrate gel combustion synthesis of ZnO Part-I: assessment of structural features. J Ceram Process Res 11:29–34
31. Xiao SH, Jiang WF, Li LY, Li XJ (2007) Low-temperature autocombustion synthesis and magnetic properties of cobalt ferrite nanopowder. Mater Chem Phys 106:82–87
32. Nagarajan N, Humadi H, Zhitomirsky I (2006) Cathodic electrodeposition of MnO_x films for electrochemical supercapacitors. Electrochim Acta 51:3039–3045
33. Windisch CF, Exarhos GJ, Owings RR (2004) Vibrational spectroscopic study of the site occupancy distribution of cations in nickel cobalt oxides. J Appl Phys 95:5435–5442
34. Tseng CC, Lee JL, Liu YM, Ger MD, Shu YY (2013) Microwave-assisted hydrothermal synthesis of spinel nickel cobaltite and application for supercapacitors. J Taiwan Inst Chem Eng 44:415–419
35. Nehru LC, Sanjeeviraja C (2013) ZnO nanoparticles by citric acid assisted microwave solution combustion method. J Ceram Process Res 14:712–716
36. Ganachari SV, Bhat R, Deshpande R, Venkataraman A (2012) Synthesis and characterization of nickel oxide nanoparticles by self-propagating low temperature combustion method. Recent Res Sci Technol 4(4):50–53
37. Wang H, Holt CMB, Li Z, Tan X, Amirkhiz BS, Xu Z, Olsen BC, Stephenson T, Mitlin D (2012) Graphene–nickel cobaltite nanocomposite asymmetrical supercapacitor with commercial level mass loading. Nano Res 5(9):605–617
38. Gautier JL, Rios E, Gracia M, Marco JF, Gancedo JR (1997) Characterisation by X-ray photoelectron spectroscopy of thin $Mn_xCo_{3-x}O_4$ ($1 \geq x \geq 0$) spinel films prepared by low-temperature spray pyrolysis. Thin Solid Films 311:51–57
39. Wang X, Han X, Lim M, Singh N, Gan CL, Jan M, Lee PS (2012) Nickel cobalt oxide-single wall carbon nanotube composite material for superior cycling stability and high-performance supercapacitor application. J Phys Chem C 116:12448–12454
40. Meher SK, Rao GR (2011) Ultralayered Co_3O_4 for high-performance supercapacitor applications. J Phys Chem C 115:15646–15654
41. Jiang H, Ma J, Li C (2012) Hierarchical porous $NiCo_2O_4$ nanowires for high-rate supercapacitors. Chem Commun 48:4465–4467
42. Vijayakumar S, Nagamuthu S, Muralidharan G (2013) Supercapacitor studies on NiO nanoflakes synthesized through a microwave route. ACS Appl Mater Interfaces 5: 2188–2196
43. Meher SK, Rao GR (2011) Effect of microwave on the nanowire morphology, optical, magnetic, and pseudocapacitance behavior of Co_3O_4. J Phys Chem C 115:25543–25556